ELSEVIER

Magnetic Resonance Imaging 21 (2003) 17–31

MAGNETIC RESONANCE IMAGING

Water diffusion in biomedical systems as related to magnetic resonance imaging

K. Khanafer[a], K. Vafai*[,a], A. Kangarlu[b]

[a]*Department of Mechanical Engineering, University of California, Riverside, CA, 92521 USA*
[b]*Advanced Center for Biomedical Imaging, Department of Radiology, The Ohio State University, Columbus, OH 43210 USA*

Received 24 June 2002; accepted 2 October 2002

Abstract

Water diffusion within the brain is studied numerically for various clinical conditions. The numerical procedure used in this work is based on the Galerkin weighted residual method of finite-element formulation. A wide range of pertinent parameters such as Lewis number, cell volume, and the buoyancy ratio are considered in the present study. Comparisons with previously published work show excellent agreement. The results show that the diffusion coefficient, cell volume, and the buoyancy ratio play significant roles on the characterization of the mass and heat transfer mechanisms within the cell. Concentration maps are developed for various clinical conditions. Pertinent results for the streamlines, isotherms and the mass and heat transfer rates in terms of the average Sherwood and Nusselt numbers are presented and discussed for different parametric values. Experimental tests are also conducted to produce an 8 Tesla image which is compared with our numerical simulation. The present study provides essential maps for brain disorders classified based on several pertinent clinical attributes.

Keywords: Diffusion coefficient; Diffusion-weighted MR imaging; Brain disorders; Transport

1. Introduction

Magnetic Resonance Imaging (MRI) has become an increasingly important tool in various applications of interest such as clinical diagnostic radiology, porous materials characterization and phase change and dynamics of compounds confined within porous media [1]. The application of MRI also extends to studies of soil water transport [2–4]. In recent years, the bulk of the research work in the literature is focused on the applications of the Magnetic Resonance Imaging as related to several clinical applications, notably in the detection of acute ischemia, brain diseases such as neurodegenerative and metabolic conditions, infections, and tumors. Different methods have been used in the past for the detection of ischemic brain tissue such as T_2-weighted nuclear magnetic resonance imaging. The main drawback of this method is the dependence of T_2 prolongation on the rather slow net increase in tissue water that develops several hours after the ischemic insult [5,6]. In order to improve diagnosis and monitor therapy of acute and transient cerebral ischemia, it would be useful to develop an imaging technique that could detect early ischemic injury and provide information regarding its localization and severity.

Recently, diffusive-weighted Magnetic Resonance Imaging has shown superior capabilities compared to other imaging methods because the ischemic brain tissue can be visualized within a very short time period. This technique is primarily due to the water diffusion process. The random molecular motion due to thermal energy is responsible for diffusion in gases and liquids. Diffusion weighted imaging, DWI, is a NMR-based technique [7,8] capable of studying the molecular displacement with microscopic accuracy. While the most commonly used method in DWI is pulsed magnetic field gradient (PFG) spin echo, PFGSE, we intend to explore possibility of developing more diffusion sensitizing (DS) pulse sequences. Safe exposure of human subjects to a field of 8T and the increase in signal to noise of such high field MRI scanners has created an opportunity to produce in-vivo human images with very high resolution [9]. As the limit of human imaging stands at 8 Tesla realistic hopes exit to push the limits of resolution to microscopic level. As such, DWI with its capability of detecting sub-pixel scale events further increases the chance of achieving true in-vivo human mi-

* Corresponding author. Tel.: +1-909-787-2135; fax: +1-909-787-2899.
E-mail address: vafai@engr.ucr.edu (K. Vafai).

0730-725X/03/$ – see front matter
PII: S0730-725X(02)00632-X

Nomenclature

D	Diffusion coefficient
e_r, e_ϕ	unit vectors in the radial and angular directions, respectively
$\vec{g}$	gravitational acceleration vector
Gr_C	solutal Grashof number, $g\beta_C\Delta C' r_o^3/\nu^2$
Gr_T	Grashof number, $g\beta_T\Delta T r_o^3/\nu^2$
k	thermal conductivity
Le	Lewis number, α/D
N	buoyancy ratio, $\frac{\beta_C\Delta C'}{\beta_T\Delta T} = \frac{Gr_C}{Gr_T}$
$\overline{Nu}$	average Nusselt number
P	dimensionless pressure
Pr	Prandtl number, ν/α
r_i	inner cylinder radius
r_o	outer cylinder radius
R	radii ratio, r_o/r_i
R_a	Rayleigh number, $g\beta\Delta T r_o^3/\nu\alpha$
Sc	Schmidt number, ν/D
$\overline{Sh}$	average Sherwood number
t	time
T	temperature
u,v	nondimensional velocity components in the radial and angular directions, respectively.
u	velocity vector
x,y	Cartesian coordinates
X,Y	dimensionless coordinates
Greek Symbols	
α	thermal diffusivity
β_T	thermal expansion coefficient
β_C	solutal expansion coefficient
ρ_o	density at reference temperature
ϕ	angular coordinate
ψ	steam function
θ	dimensionless temperature, $(T - T_o)/(T_i - T_o)$
ν	kinematic viscosity
Subscripts	
i	inner cylinder
o	outer cylinder

croscopy (ivhm). Techniques such as q-space MRI are among the early generation of techniques to enable ivhm.

Presence of various in-vivo processes such as concentration gradients offers an opportunity to study intermolecular interactions. The transport coefficients, which are the coefficient of proportionality between the corresponding flux and force is a valuable quantity to measure. Any deviation of the molecular distribution function from its equilibrium value can be acquired through measurement of these transport coefficients. Any pathology that affects the intermolecular interaction energy could be studied through its relationship with transport coefficients. In this regard the kinetic theory of gases and molecular scattering theory could be invoked to find these relationships with transport coefficients. It is important to calculate these relationships for simple models in which one could assume that relative velocities of colliding molecules are the deciding factor in determining the transport coefficients. This model could further evolve by taking into account the molecular rotational angular moment. Presence of magnetic field and its precessionl effect on angular moment process causes a small magnetic-field dependent effect on the transport properties. These small magnetic-field effects offer a sensitive tool to explore the anisotropy of the intermolecular interaction.

The importance of understanding the diffusion process in NMR stems from the fact that relaxation process is governed by molecular collisions. Specifically, molecular collision affects nuclear magnetization relaxation by reorientation. As a result of this reorientation various intramolecular interactions between the nuclear spins and the molecular rotational angular momentum is modulated. As such, modeling of diffusion process is required to quantify the anisotropy of the interaction potentials which will in turn provide more accurate account of the diffusion in relaxation time calculations.

Diffusion-weighted MR imaging is a relatively new sequence reflecting molecular motion of water within the tissue, thus providing data on tissue integrity. In diffusion MRI, powerful magnetic gradients with echo planar sequences are used. This enables high-resolution images that are dependent on water diffusion. The diffusion process is evaluated in terms of the apparent diffusion coefficient (ADC). The tissue water apparent diffusion coefficient (ADC) is considered as an essential parameter in the assessment of stroke patients [10–12]. This parameter is independent of T_1- and T_2-relaxation and directly reflects intrinsic characteristics of tissue microstructure and microdynamics. The apparent diffusion coefficient changes occur in acute and chronic brain ischemia, epilepsy, and in brain tumors [13,14]. It is found that within a very short period of time after the onset of ischemia, the apparent diffusion coefficient of water molecules in brain tissues decreases substantially. This appreciable reduction in the diffusion coefficient allows the extent of the affected area to be determined first by the diffusion-weighted magnetic resonance imaging before it can be detected using more conventional imaging modalities.

Because of the clinical importance that diffusion-weighted imaging is likely to have in early detection of stroke; a detailed understanding of the factors that affect ADC of water in tissue is of considerable importance. One study argued that the ADC drop in stroke is due to an increase in the tortuosity of the available pathways for fast diffusion within the extracellular space [15]. Another one reasoned that the decrease could be due to the cell swelling, which causes water molecules to move from extracellular space to the intracellular space, where the diffusion process may be slower, so, the overall ADC drops [16]. The combined effects of changes in cellular volume fraction and

extra- and intercellular diffusion are concluded to results in the drop of the apparent diffusion coefficient [17].

The nature of molecular diffusion of biologic samples is not very well understood. Considering complex mechanisms in action within these tissues is necessary to model diffusion contrast with account of the thermal processes distinct from magnetic field inhomogeneities, i.e., susceptibilities. Such modeling will subsequently be utilized using special experimental techniques, such as polarity reversed DS gradients to explore further enhancement of DWI sensitivity. These techniques combined with high-resolution nature of DWI at high fields have the potential of detecting minute pathologic changes in the brain [18]. Still, extensive mathematical work is required to fully exploit the sensitivity of DWI by modeling the PFG-MR correlation with the attenuation of echo signal to account for diffusion [19–21]. The possibility of q-space [22] signal enhancement compared to *k*-space signal acquisition will enable us to do very high resolution NMR. Understanding of the DWI invoking comparative inelastic scattering theory will further enhance its application to in vivo studies of tumors at much higher resolutions. Apparent diffusion coefficient (ADC) as a means for evaluation of diffusion anisotropy takes into account the various aspects of water motion in biologic tissues. Abnormal water diffusions could be detected using these methods due to their high sensitivity at high magnetic fields [23] as is done in rat brain at 7T. While application of the DWI to ischemia is well under way a similar utilization for human tumors has to await well-crafted animal studies. Characterization of tumors by diffusion techniques have just begun [24,25] and possibility for diffusion-based differentiation of tumors according to their cellularity and vascularity and possibility dynamic changes as a result of therapy related dynamic makes its future very promising.

Theoretical models for water transfer in tissues have received less attention by researchers. Greater part of the research related to water transfer in tissues has been experimentally based. The aim of the present study is to investigate water transfer process in a brain tissue numerically for various medical conditions. This model will improve the performance of the Magnetic Resonance Imaging and lead to the development of a more robust imaging system. Moreover, this study also aims at a detailed prediction of concentration maps under various clinical conditions enabling valuable medical information.

2. Problem formulation

Consider a tissue model in which the brain is represented by a two concentric cylinders. The geometry of the problem and the coordinate system are shown in Fig. 1. The fluid is contained within the cell and is assumed to be Newtonian, incompressible, and laminar. The inner cylinder of radius r_i is kept at a higher temperature and concentration (T_i and C_i') while the outer cylinder of radius r_o is kept at lower temperature and concentration (T_o and C_o'). The thermophysical properties of the fluid are assumed to be constant except the density variation in the buoyancy force, which is approximated according to the Boussinesq approximation. This variation, due to both temperature and concentration gradients, can be described by the following equation:

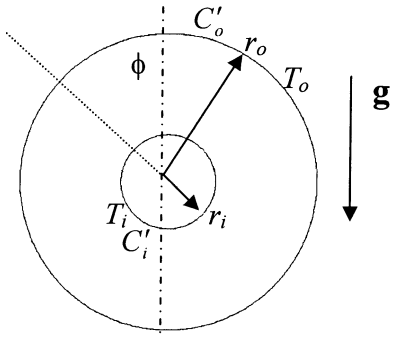

Fig. 1. Schematic of the physical model and coordinate system.

$$\rho = \rho_o[1 - \beta_T(T - T_i) - \beta_C(C' - C_i')] \tag{1}$$

where β_T and β_C are the coefficients for thermal and concentration expansions, respectively:

$$\beta_T = -\frac{1}{\rho_o}\left(\frac{\partial \rho}{\partial T}\right)_{P,C} \quad \beta_C = -\frac{1}{\rho_o}\left(\frac{\partial \rho}{\partial C'}\right)_{P,T} \tag{2}$$

To render the equations nondimensional, the following dimensionless parameters are used:

$$R_i = \frac{r_i}{r_o},\ R_o = \frac{r_o}{r_o} = 1,\ \mathrm{u} = \frac{(u,\ \mathrm{v})r_o}{\alpha\sqrt{Ra\mathrm{Pr}}},$$

$$\tau = \frac{t\alpha\sqrt{Ra\mathrm{Pr}}}{r_o^2}\ \theta = \frac{T - T_o}{T_i - T_o},$$

$$C = \frac{C' - C_o'}{C_i' - C_o'},\ P = \frac{pr_0^2}{\mu\alpha\sqrt{Ra\mathrm{Pr}}} \tag{3}$$

we arrive at

$$\nabla.\mathbf{u} = 0 \tag{4}$$

$$\frac{\partial \mathbf{u}}{\partial \tau} = -\nabla P + \frac{\nabla^2\mathbf{u}}{\sqrt{Gr_T}} + ((\theta + NC)\cos\phi e_r - (\theta + NC)\sin\phi e_\phi) \tag{5}$$

$$\frac{\partial \theta}{\partial \tau} + (\mathbf{u}.\nabla)\theta = \frac{\nabla^2\theta}{Pr\sqrt{Gr_T}} \tag{6}$$

$$\frac{\partial C}{\partial \tau} + (\mathbf{u}.\nabla)C = \frac{\nabla^2 C}{Sc\sqrt{Gr_T}} \tag{7}$$

where $\mathbf{u}$ is the velocity vector (u,v) and N is buoyancy ratio, $N = \frac{\beta_C\Delta C'}{\beta_T\Delta T} = \frac{Gr_C}{Gr_T}$, The nondimensional parameters in the above equations are Grashof number Gr_T, Gr_T

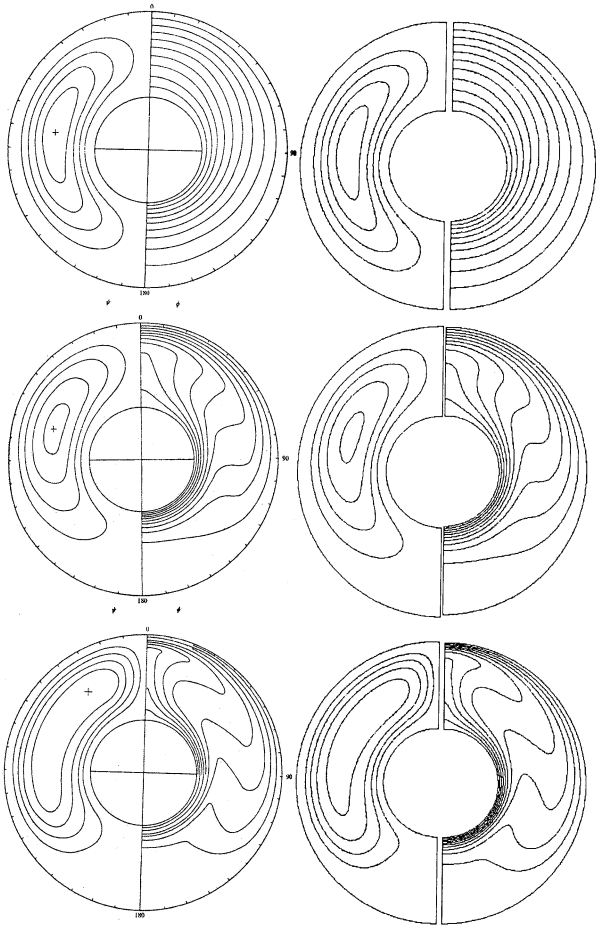

Fig. 2. Comparison of streamlines and isotherms for 2-D annuli.

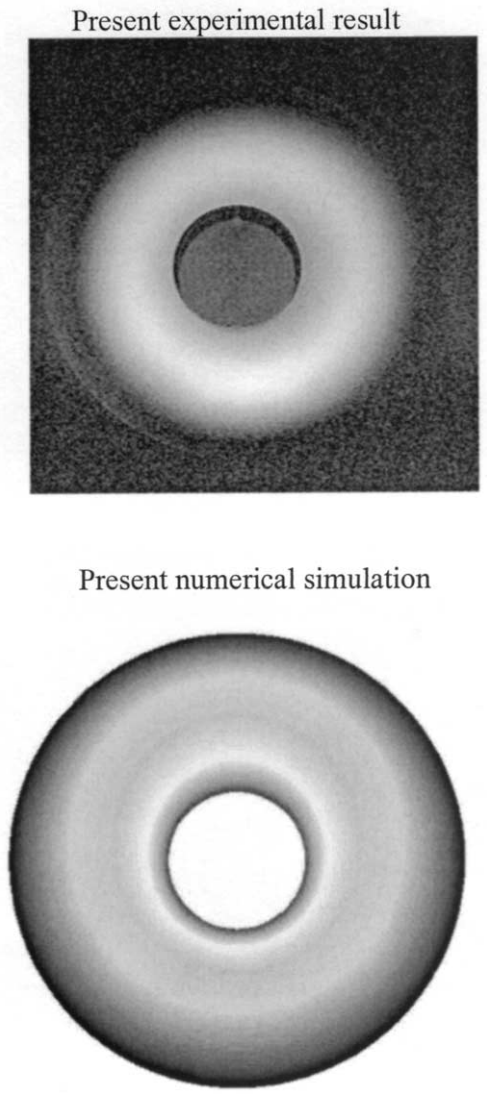

Fig. 3. Comparison of the isoconcentration contours between the present experimental and numerical results at 8T (Imaging parameters: T_R = 2000 msec, T_E = 79 msec, Δ = 46, δ = 20 msec, matrix 512).

$= \dfrac{g\beta_T(T_i - T_o)r_o^3}{\nu^2}$, the solutal Grashof number Gr_C, $Gr_C = \dfrac{g\beta_C(C_i' - C_o')r_o^3}{\nu^2}$, Prandtl number Pr, $\mathrm{Pr} = \dfrac{\nu}{\alpha}$, and Schmidt number Sc, $Sc = \dfrac{\nu}{D}$, respectively. In these equations ν, D, and α are the kinematic viscosity, diffusion coefficient, and the thermal diffusivity of the fluid, respectively.

The initial conditions for the present investigation are given by

$$u = \mathrm{v} = \theta = C = 0 \quad \text{at } t = 0 \tag{8}$$

The boundary conditions for the problem under consideration are expressed as:

$$u = \mathrm{v} = 0,\ C = \theta = 1 \quad \text{at } R_i \tag{9}$$

$$u = 0,\ \mathrm{v} = 0,\ C = \theta = 0 \quad \text{at } R_o \tag{10}$$

The local Nusselt numbers along the inner and outer cylinders are calculated as the actual heat transfer divided by the heat transfer for pure conduction in the absence of fluid motion as follows:

$$Nu_i(\phi) = -\left(R\frac{\partial\theta}{\partial R}\right)/Nu_{cond} = -\ln\frac{R_o}{R_i}\left(R\frac{\partial\theta}{\partial R}\right)_{R=R_i} \tag{11}$$

$$Nu_o(\phi) = -\left(R\frac{\partial\theta}{\partial R}\right)/Nu_{cond} = -\ln\frac{R_o}{R_i}\left(R\frac{\partial\theta}{\partial R}\right)_{R=R_o} \tag{12}$$

The average Nusselt numbers at the inner and outer cylinders are given by

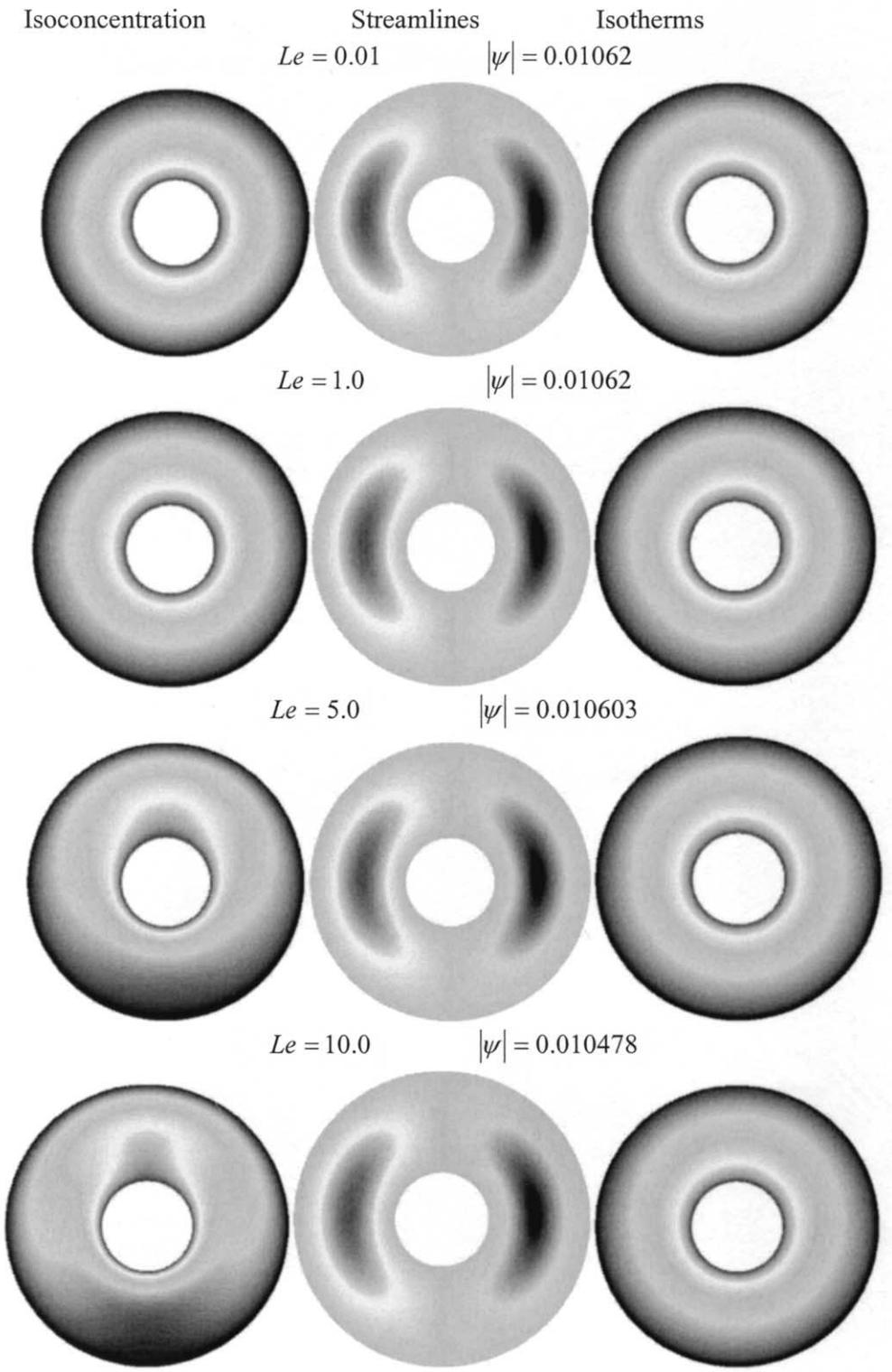

Fig. 4. Effect of the Lewis number on the isoconcentration, streamlines contours, and isotherms ($Ra = 10^3$, Pr = 5.49, $N = 0.1$).

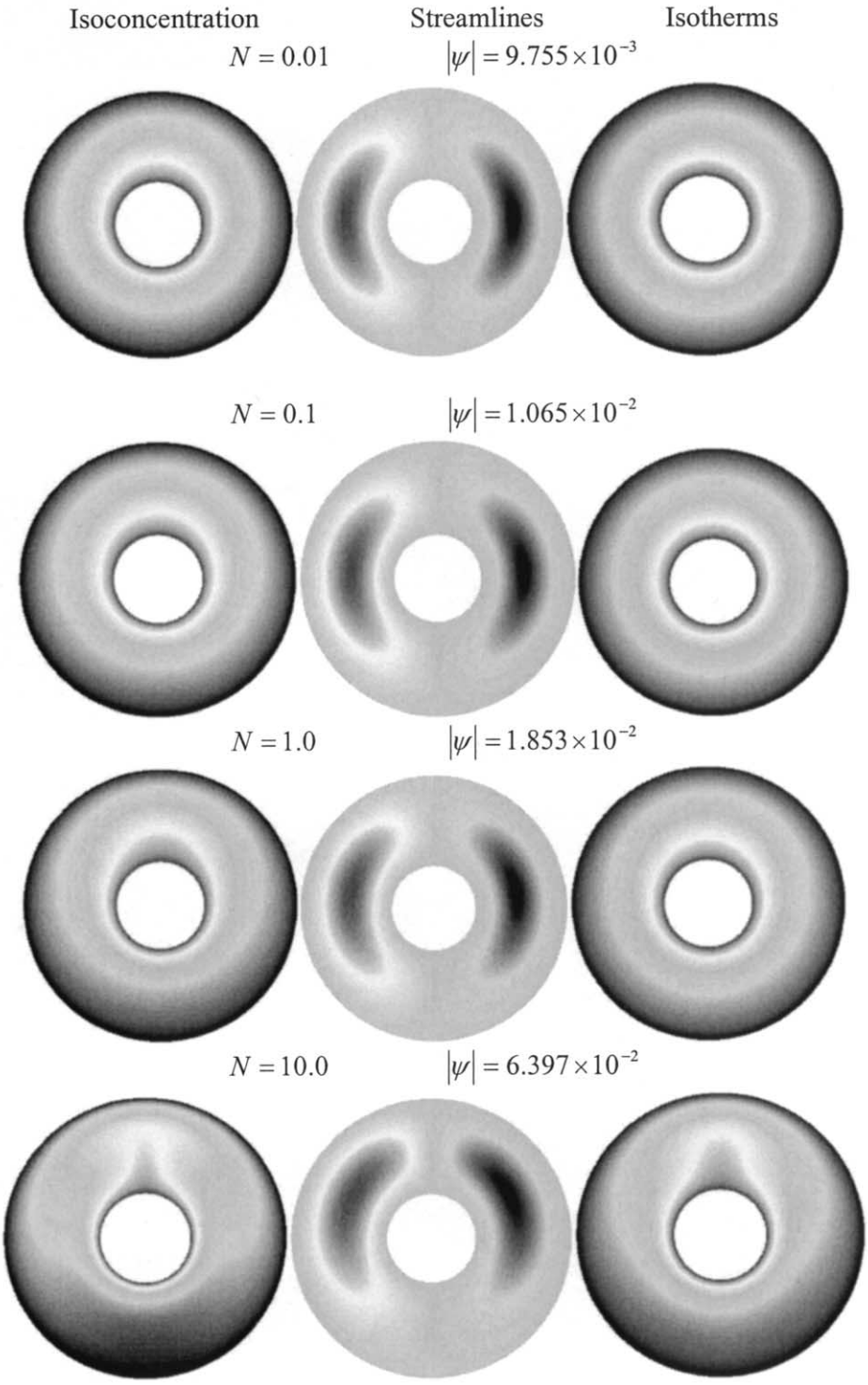

Fig. 5. Effect of the buoyancy ratio on the isoconcentration, streamlines contours, and isotherms ($Ra = 10^3$, Pr = 5.49, $Le = 2.0$).

$$\overline{Nu}_i = \frac{1}{2\pi}\int_0^{2\pi} Nu_i(\phi)d\phi$$

$$\&\overline{Nu}_o = \frac{1}{2\pi}\int_0^{2\pi} Nu_o(\phi)d\phi \quad (13)$$

Under steady state conditions, both expressions in Eq. (13), should converge to the same results.

Similarly, the average Sherwood numbers at the inner and outer cylinders are obtained as follows

$$\overline{Sh}_i = \frac{1}{2\pi}\int_0^{2\pi} Sh_i(\phi)d\phi \quad (14)$$

$$\&\overline{Sh}_o = \frac{1}{2\pi}\int_0^{2\pi} Sh_o(\phi)d\phi$$

where

$$Sh_i(\phi) = -\ln\frac{R_o}{R_i}\left(R\,\frac{\partial C}{\partial R}\right)_{R=R_i} \text{ and} \quad (15)$$

$$Sh_o(\phi) = -\ln\frac{R_o}{R_i}\left(R\,\frac{\partial C}{\partial R}\right)_{R=R_0}$$

3. Numerical method

A finite element formulation based on the Galerkin method is employed to solve the governing equations along with the boundary conditions. The application of this technique is well described by [26,27] and its application is well documented [28]. The highly coupled and non-linear algebraic equations resulting from the discretization of the governing equations are solved using an iterative solution scheme called the segregated solution algorithm. The advantage of using this method is that the global system matrix is decomposed into smaller submatrices and then solved in a sequential manner. This approach will result in substantially fewer storage requirements. The conjugate residual scheme is used to solve the symmetric pressure type equation systems, while the conjugate gradient squared is used for the non-symmetric advection-diffusion type equations. A non-uniform grid distribution is implemented in the present investigation especially near the walls to capture the rapid changes in the dependent variables. Extensive numerical experimentation was also performed to attain grid-independent results for all the field variables. The following criterion is implemented in this study to ensure the convergence of the dependent variables.

$$\frac{\|\Lambda^{n+1} - \Lambda^{n}\|_\infty}{\|\Lambda^{n+1}\|_\infty} \le 10^{-5} \quad (16)$$

where Λ is the dependent variable and n is the iteration index.

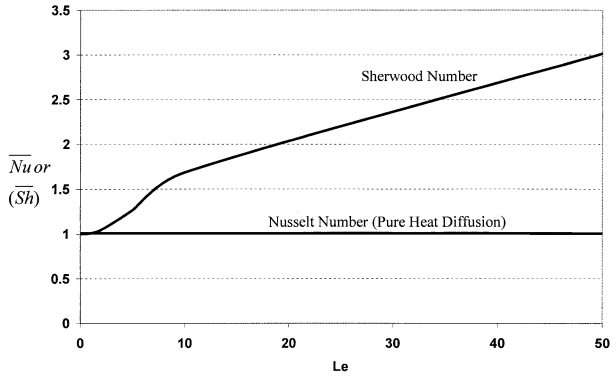

Fig. 6. Effect of the Lewis number on the average Nusselt number and Sherwood numbers ($Ra = 10^3$, Pr = 5.49, $N = 0.1$).

The present numerical approach was verified against the published results [29] for thermal natural convection within the annulus as shown in Fig. 2. It can be seen that both solutions are in excellent agreement. Moreover, the present results are compared against the present experimental work at 8T as shown in Fig. 3. The experimental image presents in Fig. 3 is part of series of ADC measurement of that yielded a $D = (1.5 \pm 0.2) \times 10^{-3}$ cm^2/s for water. The phantom is a bottle of water of 20 cm height and 10 cm diameter in the center of which a tube of 10 cm height and 3 cm diameter filled with mineral oil is located. A four port TEM RF coil was used for image acquisition. Fig. 3 shows a very good agreement between the two results.

4. Discussion of results

In this preliminary study on diffusion MRI, concentration maps are generated for different *Lewis* numbers ($Le = \alpha/D$) as shown in Fig. 4. It can be seen in this figure that for small *Lewis* number ($Le = 0.01$) or large diffusion coefficient, water transfer within the cell is totally controlled by the diffusion process. For the contours presented in Fig. 4, a very small temperature difference exists between inner

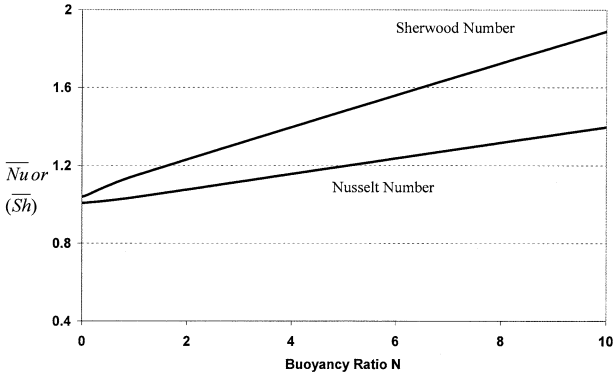

Fig. 7. Effect of the Buoyancy ratio on the average Nusselt number and Sherwood numbers ($Ra = 10^3$, Pr = 5.49, $Le = 2.0$).

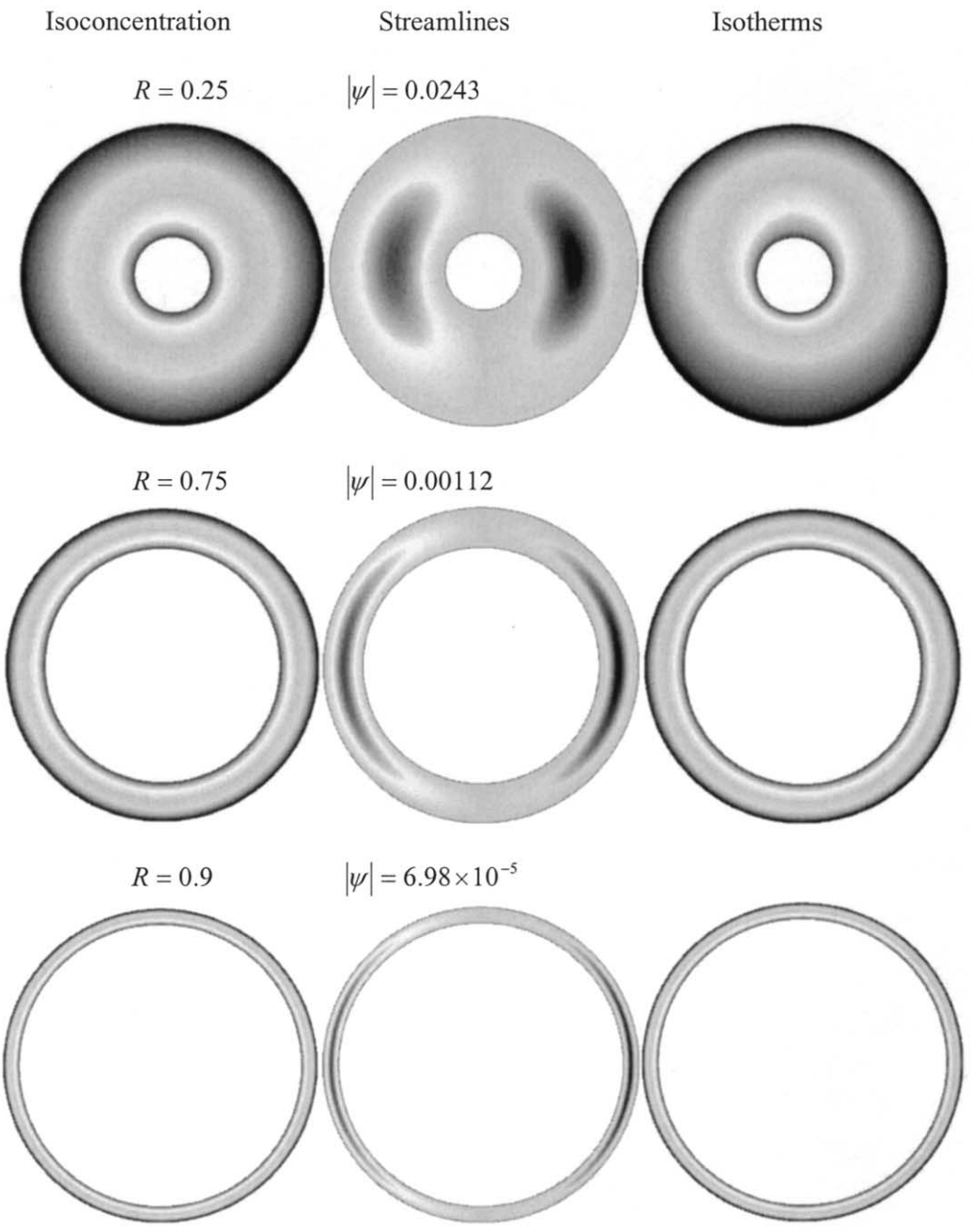

Fig. 8. Effect of the cell volume on the isoconcentration, streamlines contours, and isotherms ($Ra = 10^3$, Pr = 5.49, $N = 1.0$, $Le = 0.2$).

and outer surfaces of the cell. Thus, heat transfer is purely by heat diffusion over the entire range of the *Lewis* number as illustrated by the temperature distribution shown in Fig. 4. The effect of varying the diffusion coefficient is found to have an insignificant effect on the streamlines since heat transfer occurs mainly by diffusion. As the Lewis number increases, a significant change occurs in the concentration contours due to the thinning of the mass species boundary layers as shown in Fig. 4. While the speed of diffusion process decreases ($Le \geq 5$) there is an enhancement in the thermosolutal activities within the brain. Thus, sharp concentration gradients result in high mass transfer rates. Different mass concentration distribution resulting from varying the diffusion coefficients can reflect different brain diseases such as brain ischemic and tumor. These effects can be benchmarked when comparing normal concentration areas with high and low concentration areas to catalog different diseases.

The effect of varying the concentration difference between the inner and the outer surfaces of the brain on the water diffusion process within the brain is represented by the buoyancy ratio as shown in Fig. 5. Buoyancy ratio (N) is the ratio of the concentration potential to that by thermal convection. It can be seen in Fig. 5 that, for small values of

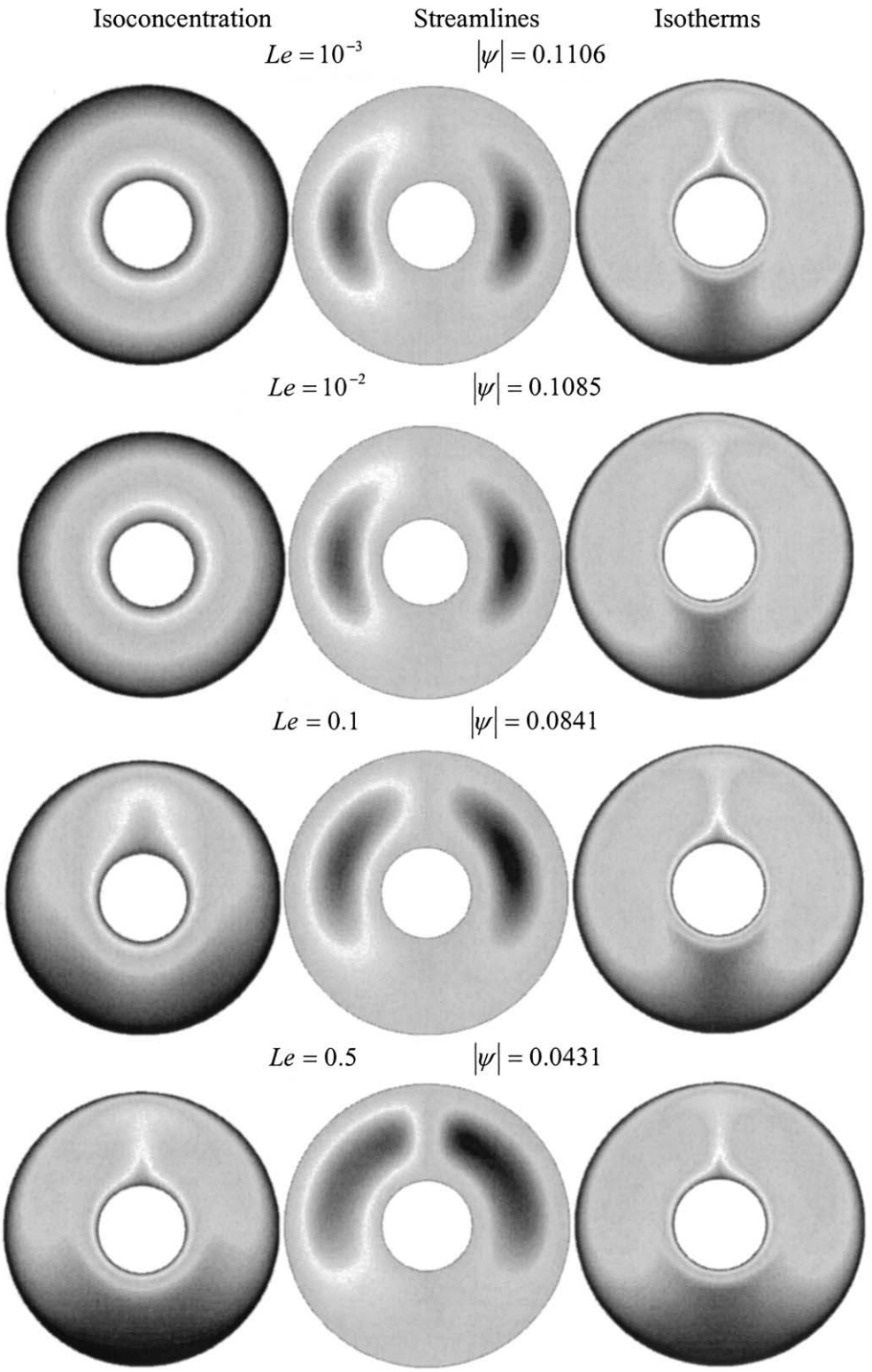

Fig. 9. Effect of the Lewis number on the isoconcentration, streamlines contours, and isotherms ($Ra = 10^5$, Pr = 5.49, $N = 1.0$).

the buoyancy ratio, the water transport process is almost entirely by diffusion. As the buoyancy ratio increases, the mass species boundary layer becomes thinner along the inner surface of the cell. This results in higher concentration gradients in the direction normal to the surface. This translates into higher heat and mass transfer rates within the brain as illustrated in Fig. 5. As a result water movement within the brain is substantially augmented as seen in the streamline contours. The high velocity regions need to be monitored carefully since it might lead to severe brain tissue

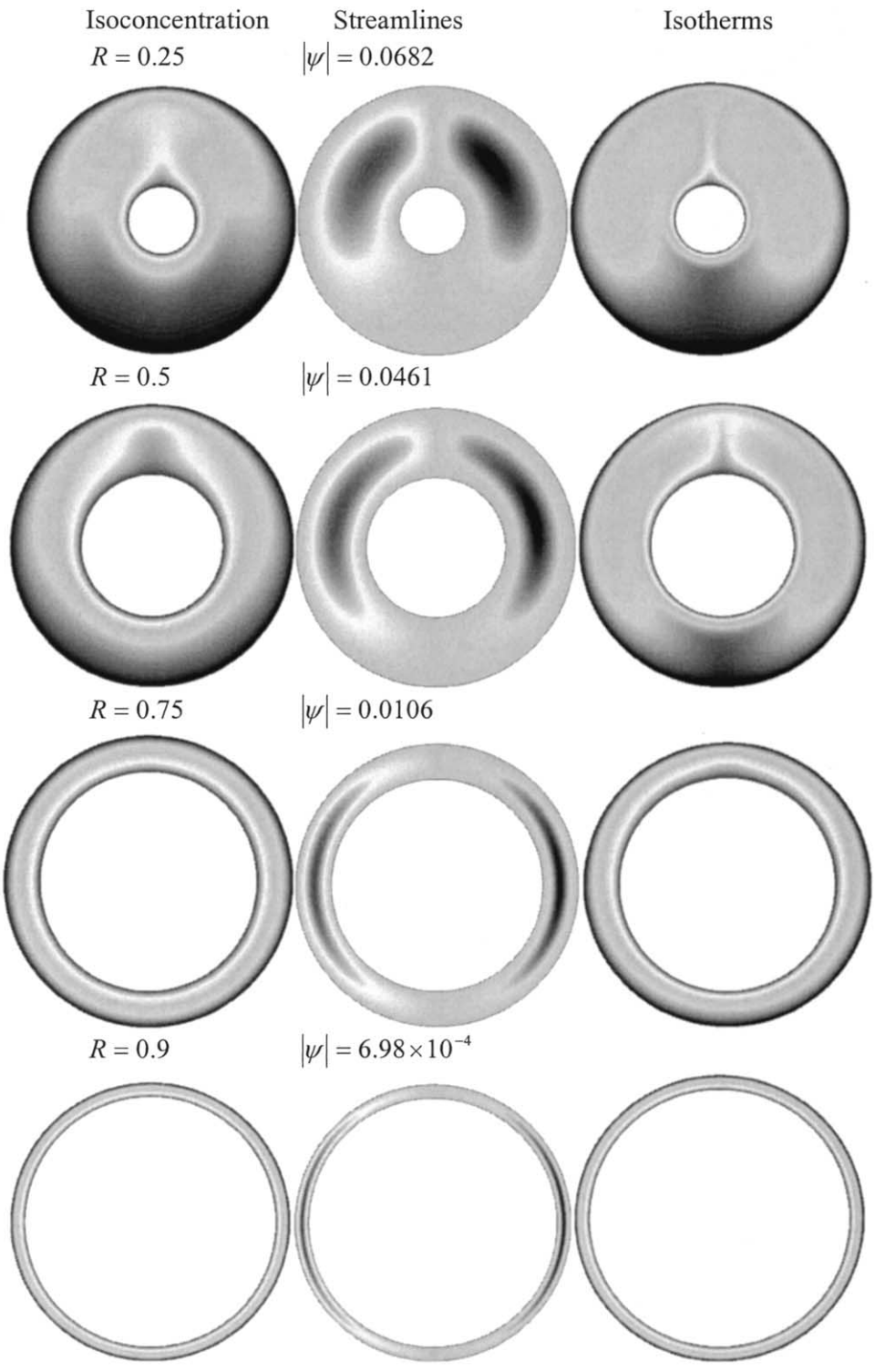

Fig. 10. Effect of the radius ratio on the isoconcentration, streamlines contours, and isotherms ($Ra = 10^5$, Pr = 5.49, $N = 1.0$, $Le = 0.2$).

damage. For large buoyancy ratios ($N = 10$), water diffusion process is replaced by the convective thermosolutal effect as shown in Fig. 5. Different concentration distributions can eventually be catalogued such that they will characterize different brain disorders.

The effect of the diffusion coefficient, D, and the buoyancy ratio, N, on the mass and heat transfer rates are shown in Figs. 6 and 7. Fig. 6 confirms that as the Lewis number increases (or the diffusion coefficient decreases), the species boundary layer thickness decreases and as a result the mass transfer rates increase rapidly and consequently the water diffusion process becomes insignificant for higher Lewis

Fig. 11. Effect of the radius ratio on the x-velocity and y-velocity components ($Ra = 10^5$, Pr = 5.49, $N = 1.0$, $Le = 0.2$).

numbers. In addition, for low Rayleigh numbers, heat transfer is primarily by diffusion as depicted in Fig. 6. The effect of varying the buoyancy ratio on heat and mass transfer rates within the brain is shown in Fig. 7 for low Rayleigh number. The results clearly indicate that an increase in the buoyancy ratio N would augment the heat and mass transfer in the cavity. This effect is more pronounced at a higher

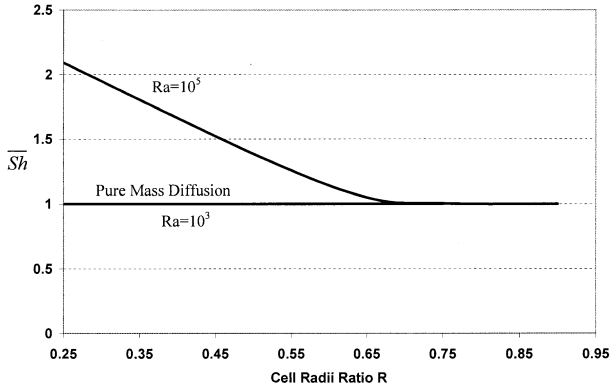

Fig. 12. Effect of the cell radii ratio on the average Sherwood number (Pr = 5.49, $N = 1.0$, $Le = 0.2$).

buoyancy ratio due to the predominant influence of the solutal buoyancy effect.

The effect of changing the brain volume on the water

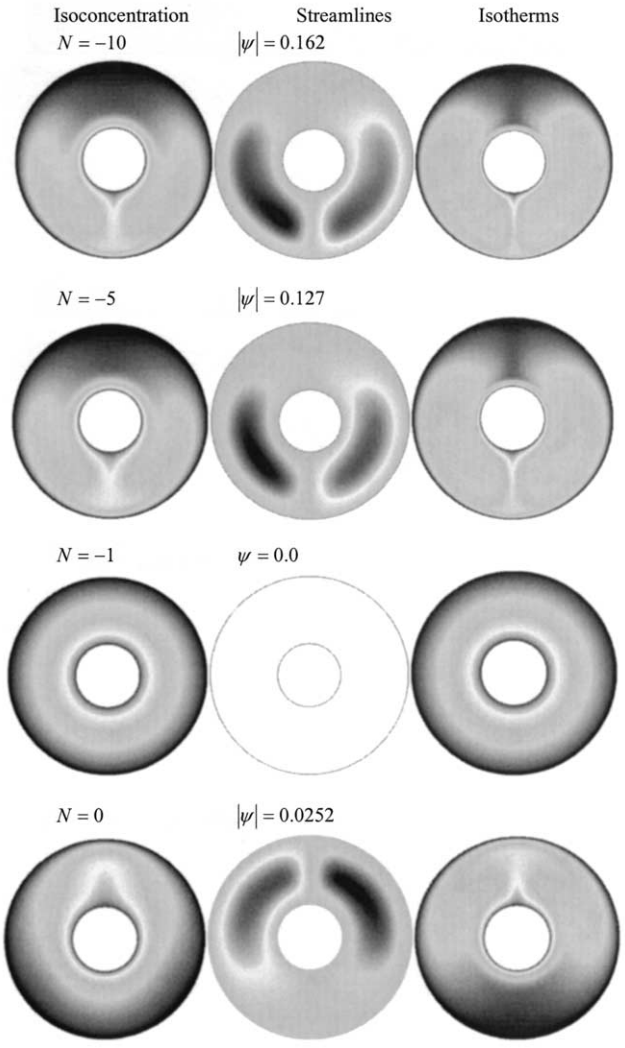

Fig. 13. Effect of the negative Buoyancy ratio on the isoconcentration, streamlines contours, and isotherms ($Ra = 10^5$, Pr = 5.49, $Le = 0.2$).

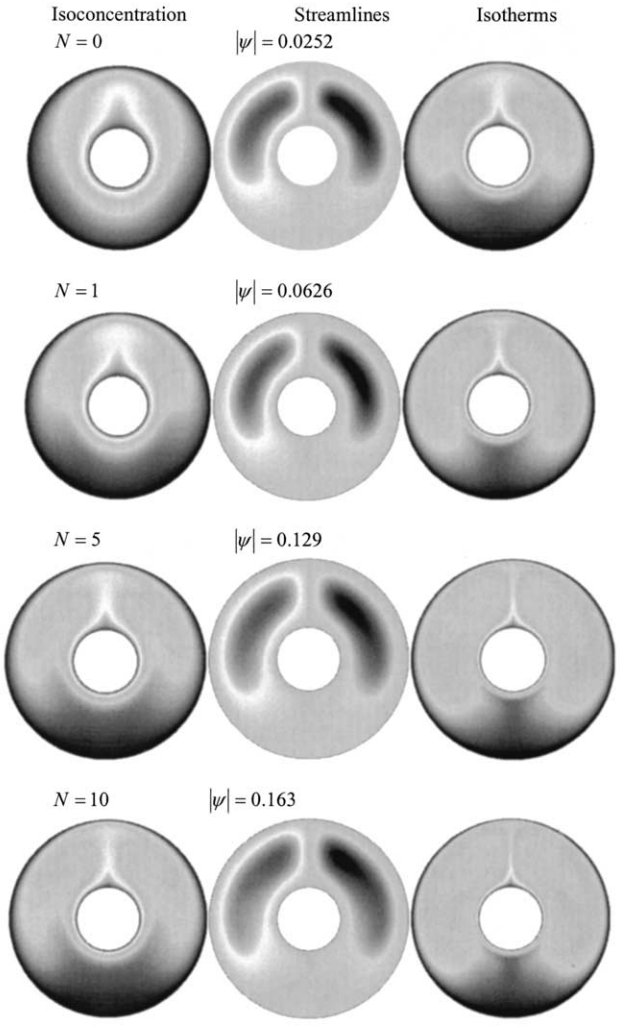

Fig. 14. Effect of the positive Buoyancy ratio on the isoconcentration, streamlines contours, and isotherms ($Ra = 10^5$, Pr = 5.49, $Le = 0.2$).

diffusion process for a low Rayleigh number ($Ra = 10^3$) and relatively large diffusion coefficient ($Le = 0.2$) is shown in Fig. 8. This effect is represented by the variation of the cell radii ratio (r_i/r_o). For the entire range of the radii ratio, the isoconcentraion contours are mainly controlled by the diffusion process within the cell. Fig. 8, also shows that the effect of combined solutal and thermal buoyancy forces is diminished for this situation indicating that these effects are overwhelmed by the diffusion process within the cell.

The effect of varying Lewis number (or the diffusion coefficient) on the concentration maps as well as the streamlines and the isotherms for high Rayleigh number ($Ra = 10^5$) is shown in Fig. 9. As the Rayleigh number increases, the intensity of natural convection within the cell increases as illustrated in Fig. 9. For small value of the Lewis number (or high diffusion coefficient), the water transport occurs mainly by diffusion. As the Lewis number increases (or the diffusion coefficient decreases), the solutal boundary layer thickness decreases resulting

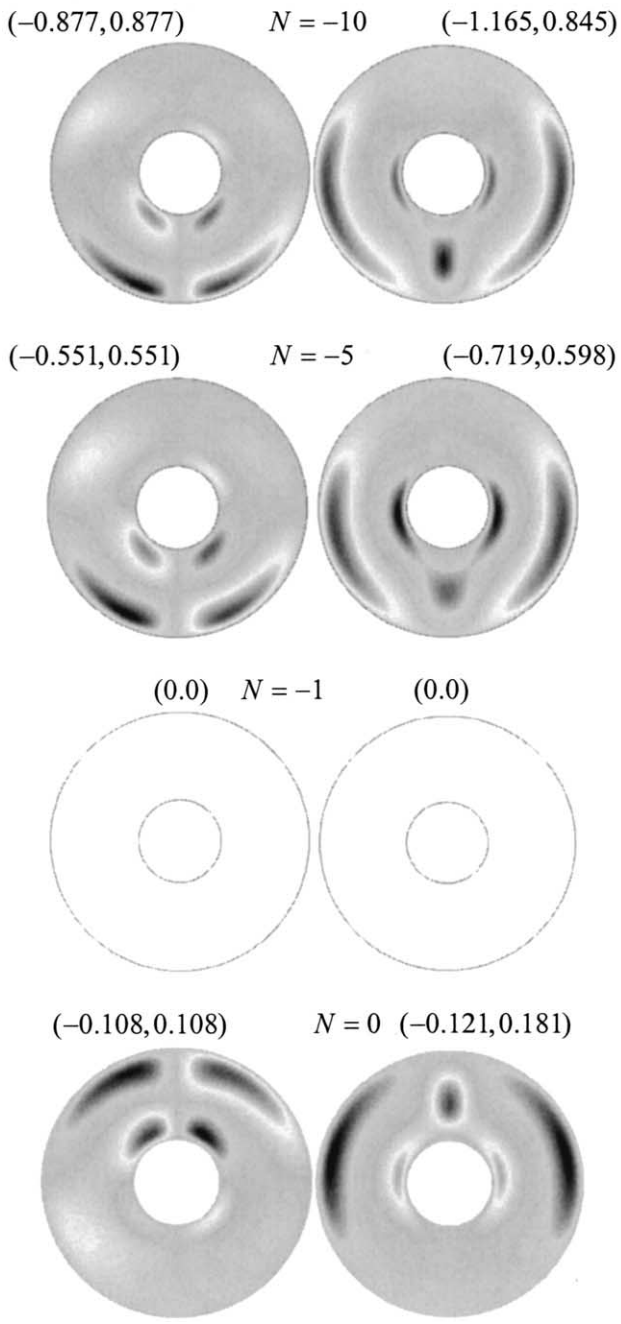

Fig. 15. Effect of the negative Buoyancy ratio on the x-velocity and y-velocity components ($Ra = 10^5$, Pr = 5.49, $Le = 0.2$).

in a mass transfer enhancement within the brain compared to the diffusion process.

The effect of changing the brain volume on the concentration maps for high Rayleigh number ($Ra = 10^5$) is shown in Fig. 10. This effect is represented by the variation of the cell radii ratio (r_i/r_o). As seen in Fig. 10, thinner mass and thermal boundary layers result in for a smaller radii ratio. As the cell radii ratio increases (or the brain volume decreases), heat and mass transfer rates are inhibited within the cell as illustrated by a significant reduction in the streamlines values at a higher cell radii ratio. As the cell radii ratio in-

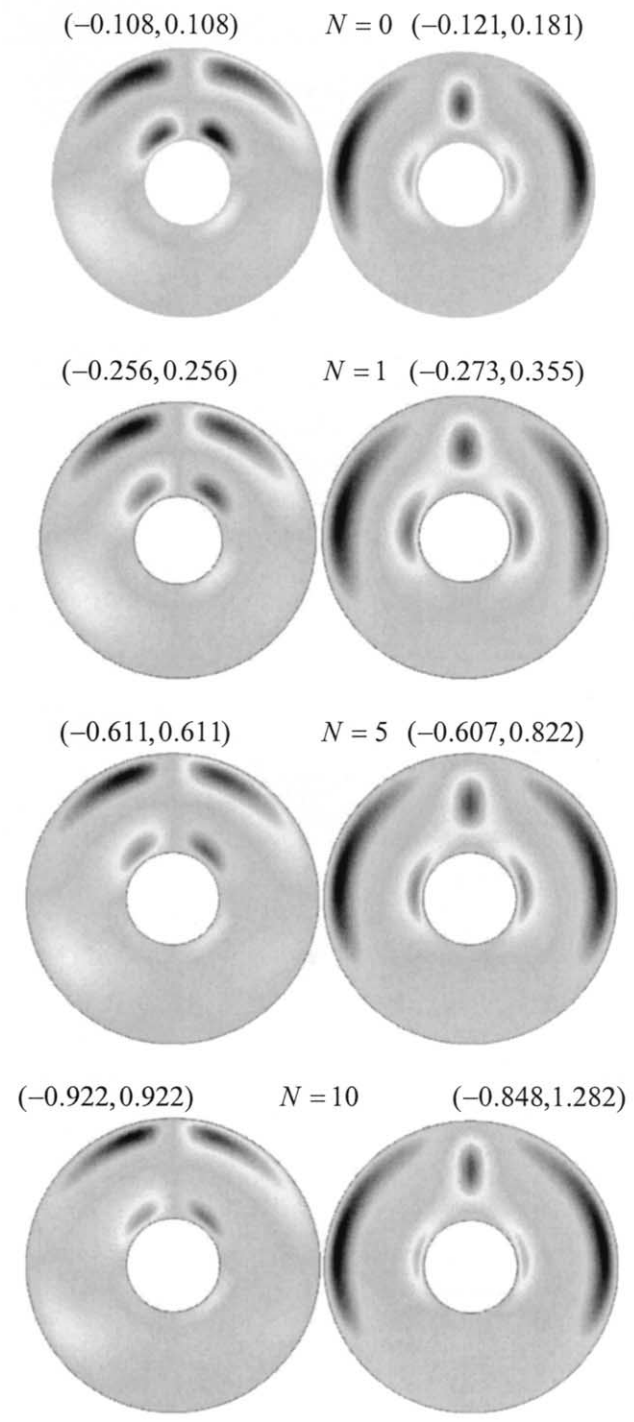

Fig. 16. Effect of the positive Buoyancy ratio on the x-velocity and y-velocity components ($Ra = 10^5$, Pr = 5.49, $Le = 0.2$).

creases, the fluid velocities diminish (Fig. 11) indicating a dominant diffusion process for high cell radii ratios.

Fig. 12 summarizes the effect of the cell radii ratio in terms of the mass transfer rate within the cell for different Rayleigh numbers. Fig. 12 illustrates that the mass transfer process is totally controlled by diffusion for small Rayleigh numbers. For a high Rayeligh number, convective mass transfer process becomes the dominant transport mechanism. However, even for a high Rayleigh number, the diffusion process is still dominant for a high cell radii ratio. These information can help in improving the imaging system in classifying different brain disorders under different clinical conditions.

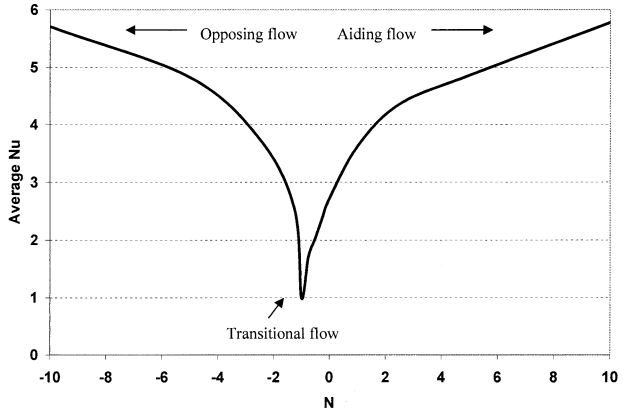

Fig. 17. Effect of the buoyancy ratio on the average Nusselt number ($Ra = 10^5$, Pr = 5.49, $Le = 0.2$).

The effect of varying the concentration between the inner and outer surfaces of the cell for high Rayleigh number and Lewis number of $Le = 0.2$ is shown in Figs. 13 and 14. For negative values of the buoyancy ratio ($N < 0$), as shown in Fig. 13, the solutal buoyancy (downward) reverses the direction of the thermal buoyancy force (upward). For larger negative values of the buoyancy ratio ($N \leq -5$) higher heat and mass transfer gradients exist in the vertical direction (downward). This scenario shows that the concentration maps are reversed in direction as a result of changing the direction of the solutal buoyancy force, indicating a different class of brain disorders.

An interesting situation is observed in Fig. 13, which is related to the buoyancy ratio $N = -1$. This situation indicates that both heat and mass transfer will cancel each other resulting in pure heat and mass transfer diffusion processes as indicated by a motionless fluid within

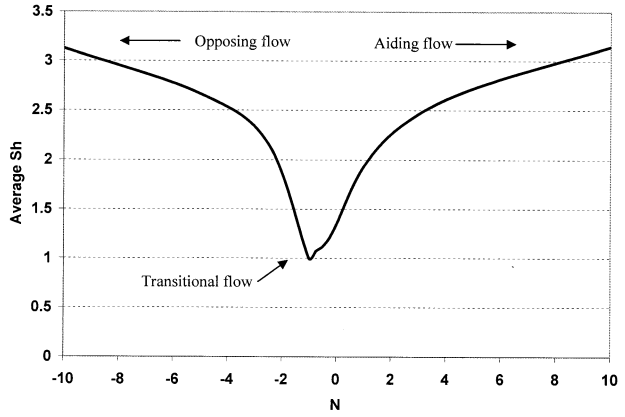

Fig. 18. Effect of the buoyancy ratio on the average Sherwood number ($Ra = 10^5$, Pr = 5.49, $Le = 0.2$).

the brain. This scenario is clearly shown in Fig. 13, which represents the velocity components at various buoyancy ratios for the middle set of figures. For buoyancy ratio $N = -1$, the velocity components are totally inhibited within the brain.

Fig. 14 shows that as the buoyancy ratio increases, the strength of the thermosolutal activities as well as the thermal convection mechanism increases resulting in higher mass and temperature gradients in the vertical direction. As a result, diffusion process is overwhelmed by the combined effects of the solutal and thermal buoyancy forces. It is evident from this Figure that as the buoyancy ratio increases the fluid velocity intensifies within the brain. This is evident in Figs. 15 and 16 where high velocity fluid motion is experienced within the cell for higher buoyancy ratios as a result of thinner mass and thermal boundary layers. This situation should be monitored carefully by an imaging system due to categorize and correlate it against the brain disorders.

Finally, the effect of the buoyancy ratio on the heat (average Nusselt number) and mass (average Sherwood number) transfer rates are shown in Figs. 17 and 18. These Figures show that the average Nusselt numbers are less in the opposing flow area ($N < 0$) than for the corresponding N in the aiding flow range ($N > 0$). This is also true for the average Sherwood number as shown in Fig. 18. Figs. 17 and 18 can be utilized to characterize various types of water transport against different types of brain disorders.

5. Conclusion

Water transfer within the brain tissue is simulated for various pertinent parameters such as cell volume, diffusion coefficient, and the ratio of the water concentration to the water thermal potential. Concentration maps for various clinical conditions are developed and analyzed in the present investigation. The present results show that, for high Rayeligh numbers, the mass transfer by diffusion is substantially diminished for small cell radii ratios. However, mass transfer by diffusion process is predominant for high cell radii ratios. In addition, the present investigation shows that certain clinical conditions can alter the diffusion coefficient within the brain tissue leading to certain categories of brain diseases. Thus, the present study helps in providing essential road maps for various brain disorders.

References

[1] Barrie PJ. NMR applications to porous solids. Ann Rep NMR Spectrosc 1995;30:37–95.

[2] Bottomley P, Rogers A, Foster TH. NMR imaging shows water distribution, and transport in plant root systems in situ. Proc Natl Acad Sci 1986;83:87–9.

[3] Liu IWY, Wong STS, Waldron LJ. The application of nuclear magnetic resonance imaging to study preferential water flow through root channels. In: Anderson SH, Hopmans JW, editors. Tomography of soil-water root processes. Madison, WI: ASA, Inc. and SSSA, Inc., 1995. p. 135–148.

[4] Amin MHG, Hall LD, Chorley RJ, Carpenter TA, Richards KS, Bache BW. Magnetic resonance imaging of soil-water phenomena. Magn Reson Imaging 1994;12:319–21.

[5] Kato H, Kogure K, Ohtomo H, Izumiyama M, Tobita M, Matsui S, Yamamoto E, Kohn H, Ikebe Y, Watanabe T. Characterization of experimental ischemic brain edema utilizing proton nuclear magnetic resonance imaging. J Cereb Blood Flow Metab 1986;6:212–21.

[6] Naruse S, Horikawa Y, Tanaka C, Hirakawa K, Nishikawa H, Yoshizaki K. Significance of proton relaxation time measurement in brain edema, cerebral infraction and brain tumors. Magn Reson Imaging 1986;4:293–304.

[7] Carr HY, Purcell EM. Effect of Diffusion on free Precession in Nuclear Magnetic Resonance Experiments. Phys Rev 1954;94:630–8.

[8] Stejskal EO, Tanner JE. Spin diffusion measurements: Spin echoes in presence of a time-dependent Field Gradient. J Chem Phys 1965;42: 288–92.

[9] Kangarlu A, Burgess RE, Zhu H, Nakayama T, Hamlin RL, Abduljalil A, Robitaille P. Cognitive, cardiac, and physiological safety studies in ultra high field magnetic resonance imaging. Magn Reson Imaging 1999;17:1407–16.

[10] Stejskal EO, Tanner JE. Use of spin-echo pulsed magnetic field gradient to study anisotropic restricted diffusion and flow. J Chem Phy 1965;43:3579–603.

[11] Taylor DG, Bushell MC. The spatial mapping of translational diffusion by the NMR imaging technique. Phys Med Biol 1985;30:345–9.

[12] Gelderen PV, DeVleeschouwer MH, DesPres D, Pekar J, VanZijl PCM, Moonen CT. Water diffusion and acute stroke. Magn Reson Med 1994;31:154–163.

[13] Lutsep HL, Albers GW, DeCrespigny A, Kamat GN, Moseley MP. Clinical utility of diffusion-weighted magnetic resonance imaging in the assessment of ischemic stroke. Ann Neurol 1997;41:574–80.

[14] Baird AE, Benfield A, Schlaug G, Siewert B, Lvblad KO, Edelman RR, Warach S. Enlargement of human cerebral ischemic lesion volumes measured by diffusion-weighted magnetic resonance imaging. Ann Neurol 1997;41:581–9.

[15] Norris DG, Niendor T, Leibfritz D. A theory of diffusion contrast in healthy, and infracted tissue, In: Proc. of SMRM, 12th Annual Meeting. New York: SMRM, 1993. p. 579.

[16] Moseley ME, Cohen Y, Mintorovitch J, Chileuitt L, Shimizu H, Kucharczyk J, Wendland MF, Weinstein PR. Early detection of cerebral ischemia in cats: comparison of diffusion and T2-weighted MRI and spectroscopy. Magn Reson Med 1990;16:330–46.

[17] Szafer A, Zhong J, Gore JC. Theoretical model for water diffusion in tissues. Magn Reson Med 1996;33:697–712.

[18] Ebisu T, Tanaka C, Umeda M, Kitamura M, Naruse S, Higuchi T, Ueda S, Sato H. Discrimination of brain abscess from necrotic or cystic tumors by diffusion-weighted echo planar imaging. Magn Reson Imaging 1996;14:1113–6.

[19] Torry HC. Bloch equation with diffusion terms. Phys. Rev 1956;104: 563–5.

[20] Stejskal EO. Use of spin echoes in a pulsed magnetic field gradient to study anisotropic restricted diffusion and flow. J Chem Phys 1965; 43:3597–603.

[21] Price WS, Kuchel PW. Effect of nonregular field gradient pulses in the stejskal and tanner (diffusion) pulse sequence. J Magn Reson 1991;94:133–9.

[22] Callaghan PT, MacGowan D, Packer KG, Zelaya FO. High resolution q-space imaging in porous structures. J Magn Reson 1990;90:177–82.

[23] Verhoye MR, S-Gravenmade EJ, Raman ER, Van Reempts J, Van Der Linden A. In vivo non invasive determination of abnormal water diffusion in the rat brain studies in an animal model for multiple

sclerosis by diffusion-weighted NMR imaging. Magn Reson Imaging 1996;14:521–32.
[24] Auer DP, Elbel GK, Jones RA. MR diffusion imaging in human braintumors, Proceeds of ISMRM, 1998; 1628: p. 324.
[25] Wiegell MR, Krabbe K, Schmieglew M, Poulsen HS, Muller J, Laursen H, Poulson OB. Diffusion anisotropy in patients treated with radiotherapy, Proceeding of ISMRM. 1998; 1341: p. 265.
[26] Taylor C, Hood P. A numerical solution of the Navier-Stokes equations using finite-element technique. Comput Fluids 1973;1:73–89.
[27] Gresho PM, Lee RL, Sani RL. On the time-dependent solution of the incompressible Navier-Stokes equations in two and three dimensions. In: Recent Advances in Numerical Methods in Fluids. Swansea, UK: Pineridge, 1980.
[28] FIDAP Theoretical Manual. Evanston, ILL: Fluid Dynamics International, 1990.
[29] Kuhen TH, Goldstein RJ. An experimental and theoretical study of natural convection in the annulus between horizontal concentric cylinders. J Fluid Mech 1976;74:695–719.